PLANETARY SCIENCE

Discovery of fossil asteroidal ice in primitive meteorite Acfer 094

Megumi Matsumoto[1]*†, Akira Tsuchiyama[2,3], Aiko Nakato[1‡], Junya Matsuno[1], Akira Miyake[1], Akimasa Kataoka[4], Motoo Ito[5], Naotaka Tomioka[5], Yu Kodama[6], Kentaro Uesugi[7], Akihisa Takeuchi[7], Tsukasa Nakano[8], Epifanio Vaccaro[9]

Carbonaceous chondrites are meteorites believed to preserve our planet's source materials, but the precise nature of these materials still remains uncertain. To uncover pristine planetary materials, we performed synchrotron radiation–based x-ray computed nanotomography of a primitive carbonaceous chondrite, Acfer 094, and found ultraporous lithology (UPL) widely distributed in a fine-grained matrix. UPLs are porous aggregates of amorphous and crystalline silicates, Fe—Ni sulfides, and organics. The porous texture must have been formed by removal of ice previously filling pore spaces, suggesting that UPLs represent fossils of primordial ice. The ice-bearing UPLs formed through sintering of fluffy icy dust aggregates around the H_2O snow line in the solar nebula and were incorporated into the Acfer 094 parent body, providing new insight into asteroid formation by dust agglomeration.

INTRODUCTION

In the early Solar System, dust grains, including ice, accreted to form planetesimals, and subsequent collisions and coalescing of planetesimals resulted in the formation of large planets. The pristine dust no longer exists in its original form in the present Solar System, but its derivatives are found in small bodies that have not grown into planets: comets and asteroids.

One of the most primitive extraterrestrial materials is a cosmic dust that originates from comets, called chondritic porous interplanetary dust particle (CP-IDP). These materials are highly porous aggregates of submicrometer-sized anhydrous silicates, Fe—Ni metals, Fe—Ni sulfides, and organics (*1*). The porous texture is thought to have been formed by the removal of interstitial ice originally present in a comet. Among the constituents, the most abundant are amorphous silicates known as glass with embedded metals and sulfides (GEMS), occurring at particle sizes in hundreds of nanometers (*2*–*4*). They are thought to represent either condensates from early Solar System nebula gases *(2)* or remnants of the amorphous silicate dust in the interstellar medium (ISM) (*3*, *4*). In infrared astronomical observations, amorphous silicates have been seen both in the ISM (*5*) and in protoplanetary disks around young stars (*6*). Irrespective of their origin, amorphous silicates and their host CP-IDPs are the pristine materials of the Solar System.

Carbonaceous chondrite meteorites are another primitive extraterrestrial material, sourced from asteroids in the inner region of the Solar System. A few extremely primitive carbonaceous chondrites have been recognized to have escaped a substantial aqueous alteration (*7*–*9*). One of these, the Paris meteorite, contains a less altered lithology, consisting mainly of loosely packed, GEMS-like amorphous silicates, although other parts of the meteorite were altered to different degrees (*8*). As possibly one of the most primitive lithologies, this meteorite preserves these source materials as a fine-grained matrix. In this study, we investigated another extremely primitive carbonaceous chondrite, Acfer 094 (*7*, *9*), to uncover evidence of asteroidal ice and pristine dust materials.

We constructed a novel analysis protocol to examine Acfer 094, systematically combining field emission scanning electron microscopy (FE-SEM), focused ion beam (FIB) microsampling, synchrotron radiation–based x-ray computed nanotomography (SR-XCT), scanning transmission electron microscopy with energy-dispersive spectroscopy (STEM/EDS), and nanoscale secondary ion mass spectroscopy (NanoSIMS; fig. S1) (see Materials and Methods). The petrographic and mineralogical analyses revealed a previously unidentified lithology exhibiting a highly porous texture widely distributed in this meteorite. The lithology is mineralogically similar to CP-IDPs and likely represents fossil icy dust aggregates, which were formed in the solar nebula before the Acfer 094 parent body formation. By combining these findings with recent theoretical studies, we here present a new model where the Acfer 094 parent body, ostensibly a planetesimal, formed by icy dust agglomeration in the early Solar System.

RESULTS

Discovery of ultraporous lithology in the fine-grained matrix

We used two polished Acfer 094 sections as samples (fig. S2). They consist mainly of coarse-grained chondrules, Ca—Al–rich inclusions (CAIs), and various mineral fragments embedded in a fine-grained matrix. The matrix [~60 volume percent (volume %)] shows a compact texture consisting mainly of submicrometer- to micrometer-sized amorphous and crystalline silicates and Fe—Ni sulfides.

After a detailed FE-SEM observation, we made two equant samples (~25 × 25 × 30 μm) from representative matrix regions using FIB. The samples were analyzed using SR-XCT at SPring-8, a synchrotron facility in Hyogo, Japan. We used two different methods: dual-energy tomography (DET) (*10*) and scanning imaging x-ray microtomography

[1]Division of Earth and Planetary Sciences, Kyoto University, Kyoto 606-8502, Japan. [2]Research Organization of Science and Technology, Ritsumeikan University, Shiga 525-8577, Japan. [3]Guangzhou Institute of Geochemistry, Chinese Academy of Sciences, Guangzhou, GD 510640, China. [4]National Astronomical Observatory of Japan, Tokyo 181-8588, Japan. [5]Kochi Institute for Core Sample Research, Japan Agency for Marine-Earth Science and Technology (JAMSTEC), Kochi 783-0093, Japan. [6]Marine Works Japan Ltd., Kanagawa 237-0063, Japan. [7]Japan Synchrotron Radiation Research Institute, Hyogo 679-5198, Japan. [8]Geological Survey of Japan, National Institute of Advanced Industrial Science and Technology, Ibaraki 305-8567, Japan. [9]Department of Earth Sciences, Natural History Museum, London SW7 5BD, UK.
*Corresponding author. Email: m_matsumto@tohoku.ac.jp
†Present address (primarily responsible for media coverage): Department of Earth and Planetary Materials Science, Tohoku University, Miyagi 980-8578, Japan.
‡Present address: Institute of Space and Astronautical Science, Japan Aerospace Exploration Agency, Kanagawa 252-5210, Japan.

(SIXM) (see Materials and Methods) (*11*). In the DET method, we obtained three-dimensional (3D) images with x-ray linear attenuation coefficients (LACs) at two different x-ray energies, one above and one below the K-absorption edge energy of iron (7.11 keV): 7 and 8 keV. The images at 7 keV corresponded closely to compositional (*Z*) contrast (Fig. 1A), and those at 8 keV strongly depended on Fe content, thus emphasizing Fe-rich materials (Fig. 1B). In the SIXM method, we simultaneously obtained images of both x-ray absorption contrast with LACs and x-ray phase contrast with refractive index decrements (RIDs). RID is simply the difference between the refractive index and unity and corresponds to material density (Fig. 1C). These computed tomography (CT) images revealed three extremely porous regions in the two samples at scales of tens of micrometers. Hereafter, we call these regions ultraporous lithology (UPL) (Fig. 1, A to C). UPLs located below the polished surface (see Fig. 1, A to C) ensure that they were originally present in the Acfer 094 meteorite. 2D histogram plots of LAC values (at 7 and 8 keV) and RID values (at 8 keV; Fig. 1, D and E) indicate that the matrix consists mainly of materials similar to hydrous phyllosilicates found in aqueously altered carbonaceous chondrites [e.g., serpentine: $Mg_3Si_2O_5(OH)_4$-$Fe_2((Si,Fe)_2O_5)(OH)_4$; saponite: $Ca_{0.25}(Mg,Fe)_3((Si,Al)_4O_{10})(OH)_2{\cdot}nH_2O$]. UPLs show darker x-ray phase contrasts than the surrounding material (Fig. 1C). The bulk densities of UPLs (1.6 to 1.9 g/cm^3) estimated from their mean RID values are lower than those of the matrix (~2.4 g/cm^3), suggesting a porosity of ~20 to 30%.

The existence of UPLs in the randomly chosen CT samples strongly suggests their wide distribution in the matrix. We thoroughly surveyed the polished surfaces of the Acfer 094 sections by FE-SEM and found numerous "candidate UPL" porous regions (e.g., Fig. 2). They are small in size (median diameter, ~11 μm; fig. S3) and distributed more or less homogeneously in the matrix (fig. S2, B and D). Their areal density is ~11 mm^{-2}, equating to a volumetric abundance of ~0.2 volume %. SR-XCT analyses confirmed that their textures, LACs, and RID values are similar to those of UPLs. These similarities suggest that the porous regions may be UPLs and that UPL may be an important building block of the Acfer 094 meteorite.

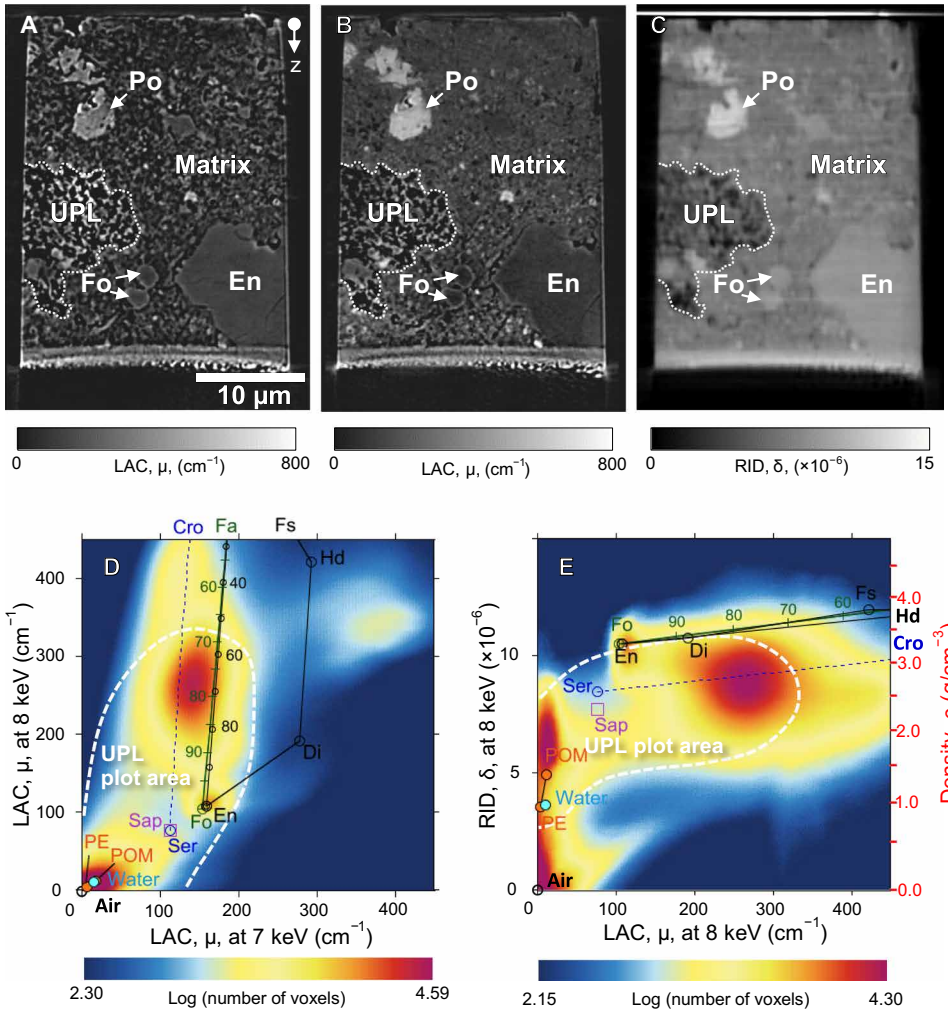

Fig. 1. XCT slice images of equant samples of the Acfer 094 matrix and their 2D histograms of LAC and RID values at 7 and 8 keV. Absorption XCT images at 7 keV (**A**) and 8 keV (**B**), as well as a phase XCT image at 8 keV (**C**), indicate an UPL embedded in the matrix. 2D histograms of LAC values at 7 and 8 keV (**D**) and LAC and RID values at 8 keV (**E**) of the matrix show peaks around the air, resin [polyacetal (POM)], forsterite (Fo), enstatite (En), and serpentine/saponite (Serp/Sap)–cronstedtite (Cro). Those plots of UPL have peaks in the areas surrounded by white dashed lines in (D) and (E). The density scale corresponding to the RID values is shown in (E). Fa, fayalite; Di, diopside; Hd, hedenbergite; Fs, ferrosilite; Po, pyrrhotite; PE, polyethylene.

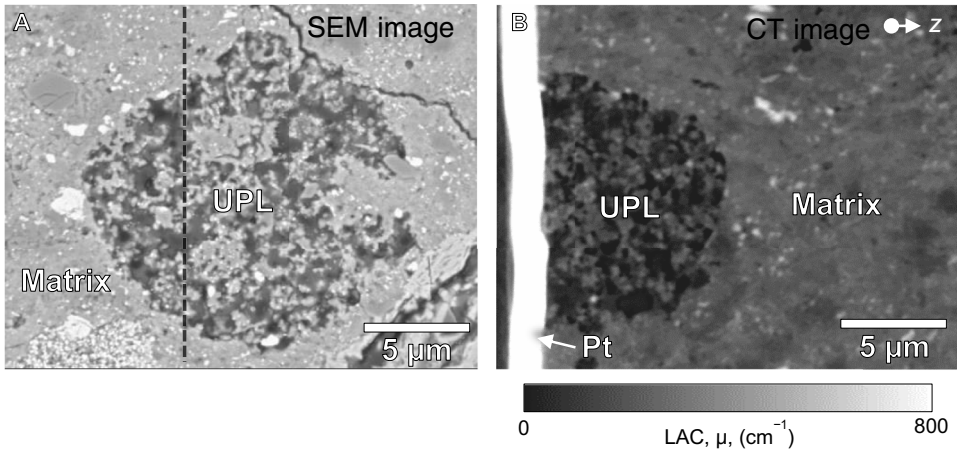

Fig. 2. SEM–back-scattered electron (BSE) and XCT slice images of a porous object on an Acfer 094 polished section surface. SEM-BSE image of the porous object (**A**) and its absorption XCT cross-sectional image along the black dashed line in (A) at 8 keV (**B**) show that the object corresponds to UPL. Pt, Pt-deposition applied during FIB sample preparation.

Mineralogy and microstructure of UPL and the matrix

We used FIB to extract two ultrathin sections containing both UPL and matrix from the two CT samples and analyzed them with TEM and NanoSIMS (Figs. 3 and 4). The porosity of UPLs estimated from TEM images (fig. S4) is ~40%, which is lower than that of CP-IDPs (>50%) (*1*). As shown in STEM elemental maps in Fig. 3 (A to C), UPLs consist mainly of fine-grained Fe—Mg–rich amorphous silicates, forsterite (Mg_2SiO_4), enstatite ($MgSiO_3$), pyrrhotite ($Fe_{1-x}S$), and pentlandite [$(Fe,Ni)_9S_8$], with spongy organics filling the pores. The Fe—Mg–rich amorphous silicates occur at scales of several hundreds of nanometers to 1 μm and are the major constituents of UPLs. They contain variable quantities of pyrrhotite and pentlandite microcrystals as inclusions, at scales of several tens to 200 nm (Fig. 4, A to C). These textures are similar to those of GEMS in CP-IDPs, but without the Fe—Ni metal inclusions common in GEMS. The GEMS-like materials analyzed here show relatively homogeneous, Fe-rich compositions compared with those of GEMS (Fig. 3D). Observed selected area electron diffraction (SAED) patterns do not show a simple halo corresponding to amorphous silicates, but rather two weak rings of *d* spacings of ~0.15 and ~0.25 nm (Fig. 4C and fig. S5). These features are similar to those of a poorly crystallized, phyllosilicate-like phase, magnesium silicate hydrate (M-S-H) (*12*). This may be the material that forms hydrous phyllosilicate-like peaks in 2D histogram plots of LAC and RID values (Fig. 1, D and E). In addition, the observed grain surfaces are partially replaced by poorly crystallized phyllosilicates (Fig. 4C). The STEM-EDS analyses also support this ostensibly hydrous nature. The GEMS-like materials in the present study show oxygen excesses compared with the number of cations detected (table S1). The water content is estimated to be 3 to 18 weight %, assuming that the excess oxygen is due entirely to H_2O in amorphous silicates (table S1). Evidence of water-rock interactions was also observed on the crystalline silicates (forsterite and enstatite): We observed these minerals often surrounded by thin rims of Fe-(hydro)oxides (Fig. 4, C and D), suggesting that Fe-rich water once existed around the silicates. It should be noted that, based on observational results in these samples, an aqueous alteration by terrestrial weathering (meteorite pollution mainly by terrestrial water) and laboratory contamination is minor.

UPLs are similar to CP-IDPs in many respects, except for the aqueous alteration (see table S2). Some enstatite grains in UPLs are whiskers elongated along the crystallographic *a* axis (Fig. 4D). These enstatite grains are common in CP-IDPs and are thought to have been formed by condensation from nebula gas (*13*). Enstatite and olivine grains in UPLs often form aggregates at scales of several hundreds of nanometers (fig. S6), which are similar to "equilibrated aggregates" in CP-IDPs. Those aggregates are thought to be formed by annealing of preexisting dust in the early solar nebula (*2*). Spongy organics filling the pores in UPLs are composed of C, N, and O, with normal (solar) oxygen isotopic compositions (Fig. 3E and table S3). These organics are also common in CP-IDPs and in other carbonaceous chondrites (*14*). All these constituents of UPLs are expected to be remnants of pristine dust in the early solar nebula. Apparently, UPL is a highly pristine lithology preserving primitive solid Solar System materials.

The surrounding matrix consists of essentially the same materials as UPLs, as shown in the STEM images and elemental maps (Fig. 3, A to C), with amorphous silicates seeming to form a continuous matrix. However, detailed TEM observations reveal that the amorphous silicates occur as discrete, submicrometer-sized grains, closely packed in the matrix (Fig. 4E). The amorphous silicates contain various quantities of pyrrhotite and pentlandite inclusions, as seen in UPLs (Fig. 4E). The characteristics of the amorphous silicates, such as crystallinity (e.g., the presence of poorly crystalized phyllosilicates or M-S-H; Fig. 4F), chemical compositions [H_2O contents: 7 to 14 weight % (wt %); Fig. 3D and table S1], and oxygen isotopic compositions (Fig. 3E and table S3), are almost the same as those for UPLs. We also observed enstatite whiskers with *a* axis elongation in the matrix (fig. S7). Organics occur widely in the matrix, although the amount is lower than that in UPLs (Fig. 3C). These strongly suggest that the matrix was formed by accretion and compaction of UPLs or related materials as the Acfer 094 parent body. The compaction of the wet amorphous silicates should have easily proceeded even at low temperature, which is consistent with the least thermally metamorphosed state of Acfer 094 (*9*).

DISCUSSION

Evidence of asteroidal ice in Acfer 094

UPLs with abundant pores are fragile. Nevertheless, UPLs show no evidence for pore compaction (Fig. 3A), which would be expected

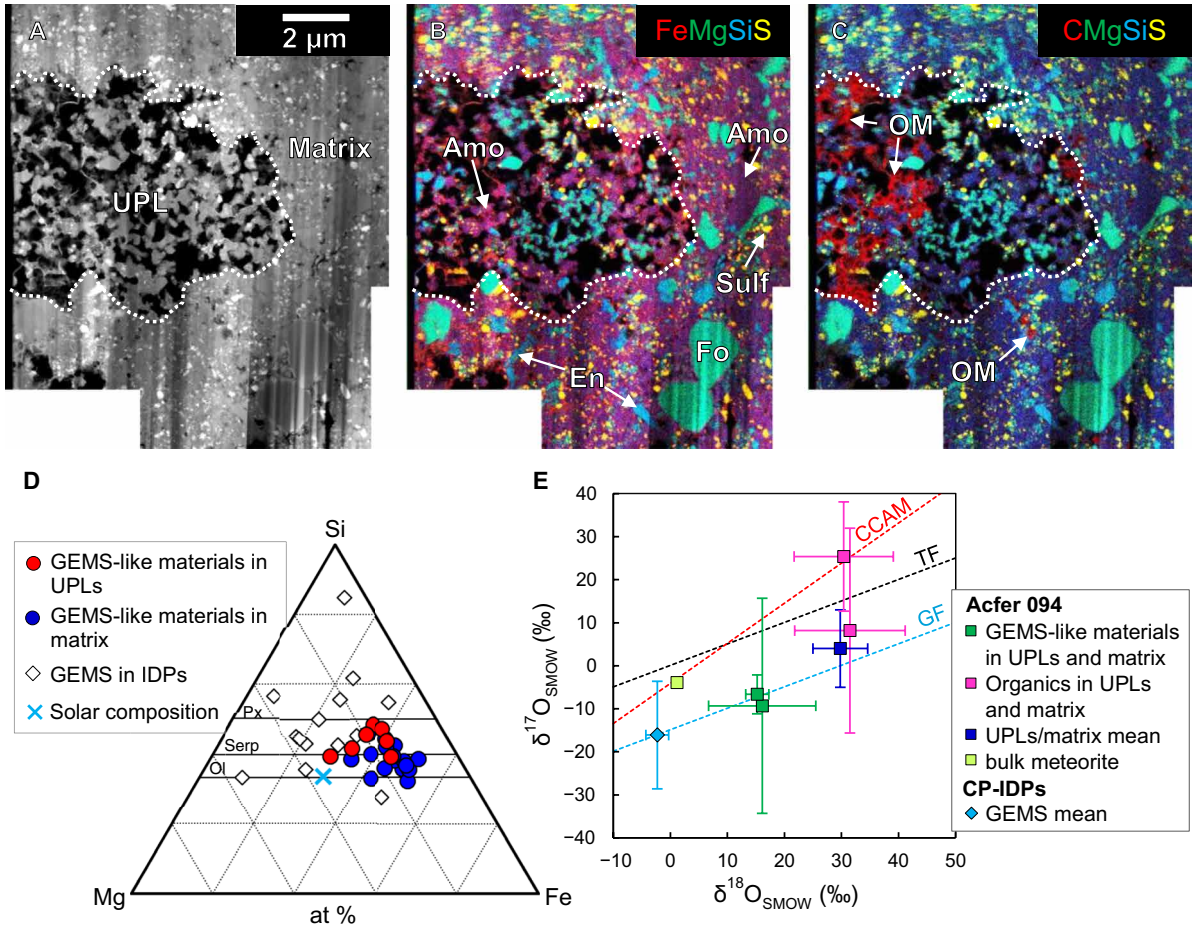

Fig. 3. STEM-EDS maps and chemical and oxygen isotopic compositions of UPL and the matrix. An annular dark field (ADF)–STEM image (**A**) and a combined STEM-EDS map (**B**) for Fe (red), Mg (green), Si (blue), and S (yellow) show that both UPL and the matrix consist mainly of amorphous silicates (Amo; magenta), forsterite (Fo; light green), enstatite (En; cyan), and Fe—Ni sulfides (Sulf; yellow). Spongy organics (OM; red) (**C**) are heterogeneously distributed in the UPL. Compositions of GEMS-like materials (Amo + Sulf) in the UPL and the matrix, plotted in the Si—Mg—Fe diagram (**D**), are relatively homogeneous and enriched in Fe compared with those of GEMS in CP-IDPs (*1*, *3*, *4*). Olivine (Ol), pyroxene (Px), and serpentine (Serp) solid solution lines are also shown in (D). at %, atomic %. The oxygen isotopic compositions of UPL and the matrix are plotted in the oxygen three-isotope diagram (**E**). GEMS-like materials in UPLs and the matrix plot around the GEMS (*2*) mass fractionation (GF) line, suggesting their similar origins. The constituents in UPLs and the matrix show relatively heavy-oxygen isotopic compositions compared with the bulk meteorite (*15*). SMOW, standard mean of ocean water; TF, terrestrial mass fractionation line; CCAM, carbonaceous chondrite anhydrous mineral line.

to have occurred during accretion. This strongly suggests that the pores in UPLs were originally filled with some solid material(s). Ice is one of the major components of cometary nuclei and should be present in the pores of cometary CP-IDPs. Therefore, it is reasonable that some ice was the original solid material, subsequently lost by evaporation and/or melting caused by an increase in temperature. That is, we interpret the pores in UPLs as fossils of primordial ice in this carbonaceous chondrite parent body. Melting of this ice is expected to have caused the observed aqueous alteration in UPLs and in the matrix. Many oxygen isotopic studies of carbonaceous chondrites have suggested that the water (ice) responsible for the aqueous alterations was rich in heavy-oxygen isotopes (*15*). The Acfer 094 meteorite contains cosmic symplectite, several-tens-of-micrometer-sized opaque nugget consisting of a very fine intergrowth of magnetite and pentlandite with the heaviest oxygen isotopic composition among the solar materials; this symplectite is thought to have been formed by interactions with heavy-oxygen water (*16*). Oxygen isotopic measurements with NanoSIMS ion imaging show that constituents of UPLs and the matrix have relatively heavy-oxygen isotopic compositions (Fig. 3E and table S3), consistent with the hypothesized interactions with water produced by melting of isotopically heavy ice. Organics might be another material that played a significant role in preserving the porous structure of UPLs. A highly primitive lithology containing abundant organics was reported in a carbonaceous chondrite, LaPaz Icefield 02342, recently (*17*). However, it is supposed that organics alone could not sustain UPLs against compaction because they were not filling all the pores in UPLs (Fig. 3, A and C). Even if we assume that the organics we observed are evaporation residues of volatile-rich organics that originally filled all the pores in UPLs, the residual refractory organics should be observed homogeneously on the surfaces of all the silicate grains in UPLs. However, the organics in UPLs do not show this distribution. In addition, it is expected that the volatile-rich organics may be compressed easily compared with solid H_2O ice, and hardly to prevent the pore compaction alone. This might be the case of the organics in the matrix, which are well compacted (Fig. 3C). Accordingly, it appears reasonable

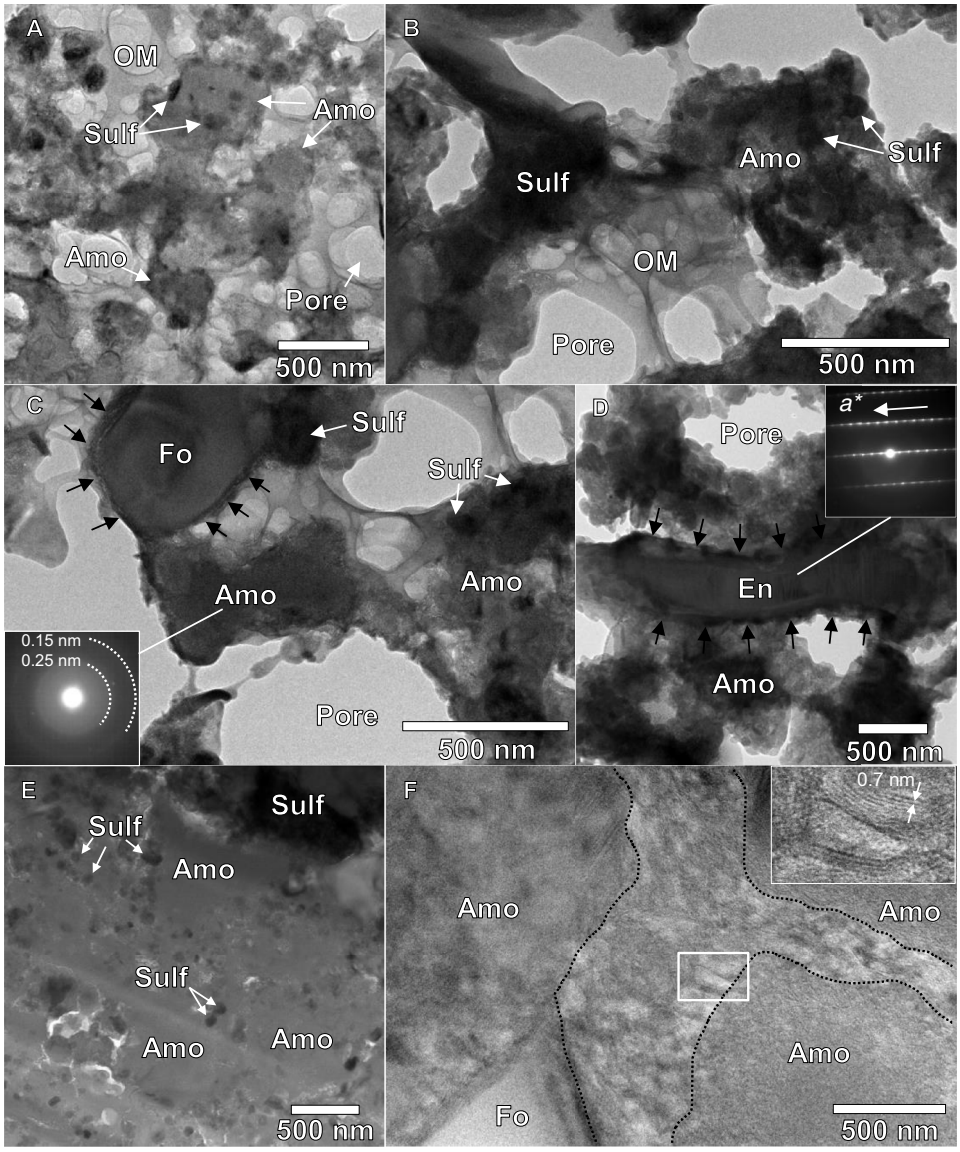

Fig. 4. Bright-field (BF)–TEM images of UPLs and the matrix. (**A** to **C**) BF-TEM images of UPLs show that amorphous silicates (Amo) contain various quantities of small Fe—Ni sulfide (Sulf) inclusions and that pores are partially filled with spongy organics (OM). The 2D SAED pattern of the amorphous silicate in (C) contains weak rings of ~0.15 and ~0.25 nm. A BF-TEM image of an enstatite (En) whisker in UPL (**D**) shows that it is elongated along the crystallographic *a* axis. The enstatite and forsterite (Fo) in (C) are surrounded by thin, Fe-rich layers, indicated by black arrows. A BF-TEM image of the matrix (**E**) shows that it mainly consists of densely packed amorphous silicates with Fe—Ni sulfide inclusions. The interspaces between the amorphous silicate grains are filled with poorly crystallized phyllosilicates with a *d* spacing of ~0.7 nm (**F**).

that ice coexisting with some organics in the pores was the major material that prevented the compaction of UPLs. It is worth noticing that the primitive lithology in LaPaz 02342 is also suggested to have originally contained some ice (*17*).

At present, a large number of aqueously altered meteorites are known. However, it has remained unknown how the ice responsible for the aqueous alteration was distributed in meteorite parent bodies. Our work suggests that UPLs, hosting the primordial ice, were distributed homogeneously in the Acfer 094 meteorite. However, the abundance of primordial ice estimated from the pore volume in UPLs is not sufficient to justify the aqueous alteration of the whole matrix. That is, some additional ice (UPL) is required to explain the water content in the Acfer 094 parent body. The required volume fraction of the ice-bearing UPL relative to the matrix at the time of the Acfer 094 parent body formation, X, is calculated as follows

$$X = (W_{H2O} \times \rho_s)/\{P \times (W_{H2O} \times \rho_s + \rho_{ice})\}$$

where P is the porosity in UPL, W_{H2O} is the water contents in the matrix in weight, ρ_s is the density of the matrix, and ρ_{ice} is the density of water ice (1 g/cm^3). Here, we assume that the matrix is not porous and consists of only amorphous silicates. On the basis of the present results (P = 0.4, W_{H2O} = 0.1, and ρ_s = ~2.4 g/cm^3), X is calculated to be 0.48. This means that roughly (ice-bearing UPLs):(solid matrix) = 1:1 is required to explain the observed water contents in the amorphous silicates (~10 wt %). This value is much higher than the observed volume (UPLs, ~0.2 volume %), indicating that the distribution of ice in the

Acfer 094 parent body, ostensibly a planetesimal, was heterogeneous and that ice was much more abundant elsewhere in the parent body, as discussed in detail below.

Formation of the Acfer 094 parent body by icy dust agglomeration

Several models have been proposed for planetesimal formation (*18*, *19*). Among these, recent theoretical studies have proposed that kilometer-sized planetesimals could be formed by simple dust growth in the protoplanetary disk (*19*). They showed that submicrometer-sized particles aggregated into fluffy dust and became larger and more porous through further accretion. These highly porous objects can overcome rapid falling of centimeter- to meter-sized solid objects into the protosun (the so-called radial drift problem) so that densely packed planetesimals can ultimately be formed mainly through static compression due to ram pressure of nebula gas and self-gravity (*20*). For the Acfer 094 parent body formation, we simply assume fluffy ice-silicate aggregate (FISA) and fluffy silicate aggregate (FSA), respectively, as source dust originally present in the outer and inner regions of the H_2O snow line (Fig. 5). Here, FISA denotes the general model of icy dust grains: a fluffy aggregate of silicate grains covered with an H_2O icy mantle (*21*). According to recent astrophysical models that explain the present Solar System configuration, including the giant planet's orbits and the distributions of Jupiter's Trojans and main-belt asteroids, our planetesimals and planets underwent substantial radial migrations in the early stage of the Solar System evolution (*22*, *23*). Acfer 094 parent body growth by FISA and FSA agglomeration during radial migration from the outer to the inner regions of the early Solar System across the H_2O snow line would produce a radial variation of ice abundance in the parent body (Fig. 5).

Recent simulations suggest that FISA suffered sintering around the H_2O snow line (*24*). The increase in temperature induced sublimation of ice, and subsequent condensation and accumulation of fragmented grains formed solid dust aggregates of silicate grains embedded in ice, which correspond to ice-bearing UPLs (*24*, *25*). The currently estimated millimeter-to-centimeter size of dust aggregates in protoplanetary disks (*26*) is much larger than the size of the observed UPLs (~11 μm). However, polarization signatures in recent Atacama Large Millimeter/submillimeter Array (ALMA) observations indicate the presence of broadly similar dust sizes (~70 μm) (*27*). In addition, sintering of fluffy dust around snow lines of different volatile compounds (e.g., CO_2) has been proposed as a key process in the formation of the multiring structures that ALMA observations have found in many protoplanetary disks (*28*, *29*).

Around the H_2O snow line, fluffy dust as a precursor of the matrix and ice-bearing UPLs accreted to the Acfer 094 parent body

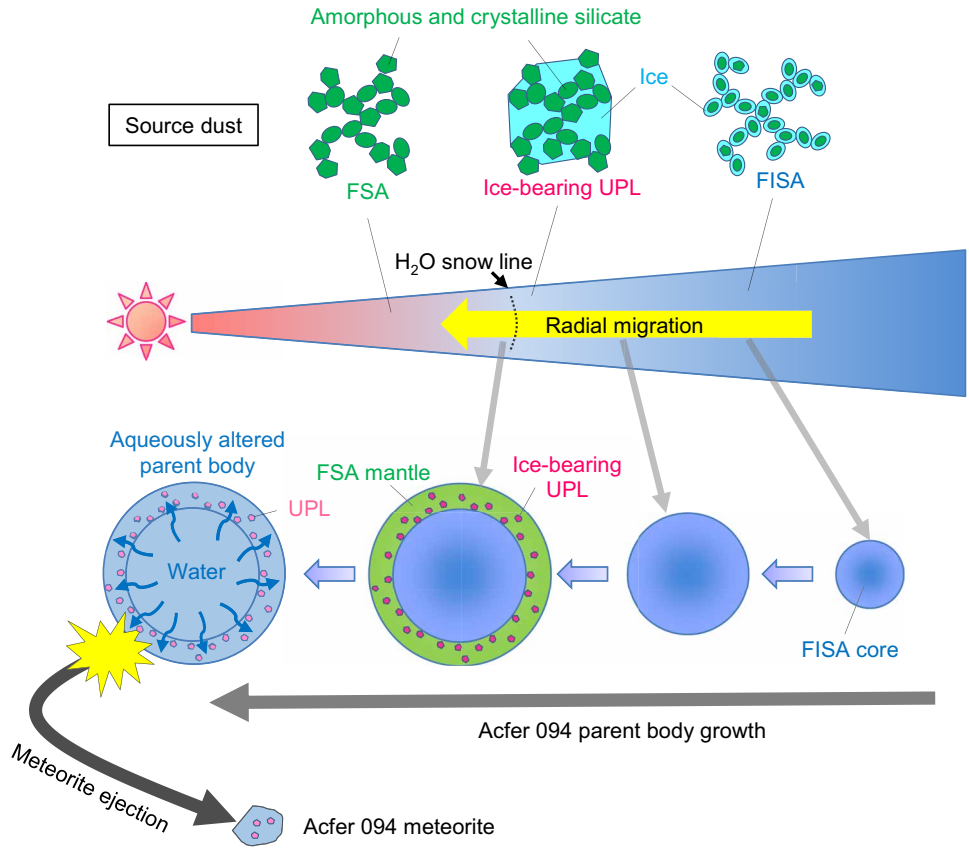

Fig. 5. Schematic illustration of the Acfer 094 parent body formation model. The parent body grew by agglomeration of fluffy source dust with and without ice through its radial migration from the outer to the inner regions of the solar nebula across the H_2O snow line. The process produced a layered structure inside the parent body, with an ice-rich core and an ice-poor mantle. Around the H_2O snow line, ice-bearing UPLs were incorporated into the mantle. Subsequently, the melting of ice, mainly in the core, induced an aqueous alteration in the parent body. The Acfer 094 meteorite was subsequently ejected from the mantle of the parent body by some destructive processes. Note that we did not describe organics, which might have existed in ice in FISA and ice-bearing UPLs to make it easier to understand. FSA might also have contained some refractory organics.

surface (Fig. 5). If the Acfer 094 parent body surface was composed of porous aggregates of fluffy dust (FSA) and ice-bearing UPLs shortly after the accretion, migration of H_2O molecules from the H_2O ice in UPLs to the neck parts between contacting solid grains in the porous aggregates would have occurred. This is because of the concave surface at the neck, which has a low-equilibrium vapor pressure of H_2O. In this case, as the total volume of the pore spaces around the necks was much larger than that of the H_2O ice in UPLs, the H_2O ice would have disappeared and could not have contributed to sustaining the UPLs. The presence of surviving UPLs means that the actual pore volume was not so large due to the fluffy dust accreting to the parent body, losing the majority of the pore spaces by compression caused by collision with the parent body surface. The compression could occur if the Acfer 094 parent body had already reached a large mass at the timing of the accretion of ice-bearing UPLs (*20*). In addition, if the fluffy dust contained a small amount of ice, most likely in the neck parts, the migration of H_2O molecules would have been more limited. These could have caused the ice-bearing UPLs to survive in the parent body at the timing of their accretion.

Subsequently, aqueous alteration occurred in the parent body, and the major source of the water would have been supplied by the ice-rich core region of the parent body in addition to the melted ice already present in the neck parts and UPLs. This alteration would have significantly reduced the interspaces among the matrix grains, since the volume of the amorphous silicate is particularly increased by hydration. If we assume the following hydration reaction of amorphous silicate

$$8\,MgSiO_3(amo) + 16\,H_2O \rightarrow Mg_8Si_8O_{20}(OH)_8 \cdot (H_2O)_{12}(M\text{-}S\text{-}H)$$

the volume ratio of the reactant amorphous silicate and the product M-S-H ($V_{M\text{-}S\text{-}H}/8V_{amo}$) is calculated to be ~2.2, where $V_{M\text{-}S\text{-}H}$ and V_{amo} are the molar volumes of M-S-H [630.90 cm^3/mol for $Mg_8Si_8O_{20}(OH)_8 \cdot (H_2O)_{12}$; (*30*)] and amorphous silicate [36.36 cm^3/mol for $MgSiO_3$; (*31*)], respectively. These processes led to the formation of an almost solid matrix without compression and, thus, without compacting the UPLs.

From the above discussions, we propose the following scenario for the Acfer 094 parent body formation (Fig. 5): (i) The parent body grew from fluffy dust with and without ice through radial migration from the outer to the inner regions of the early Solar System across the H_2O snow line. (ii) Ice-bearing UPLs formed by sintering were incorporated onto the parent body surface with fluffy dust around the H_2O snow line; this process would produce the low abundance of UPLs in the Acfer 094 meteorite. (iii) Subsequently, an aqueous alteration induced by melting of ice took place in the parent body. The meteorite's major source of water was the ice-rich core of the parent body.

Meaning of the presence of UPL-like lithology in primitive meteorites

The present scenario is a practical model to give new insight into asteroid formation by combining both analytical results of extraterrestrial materials and theoretical models of planetesimal formation. According to the present model, the discovery of UPLs in any chondrite implies that its parent body formation crossed the snow line. UPL-like porous lithology in the Paris meteorite (see table S2) (*8*) is one such candidate and might have been formed by fluffy dust sintering. The CO_2 snow line in the outer region of the H_2O snow line might be considered for the formation of porous lithologies if the radial migration of planetesimals is taken into consideration.

MATERIALS AND METHODS

Experimental design

To obtain a thorough petrographic and mineralogical characteristics of the Acfer 094 meteorite, we performed systematic analyses combining FE-SEM, FIB microsampling, SR-XCT, FE-TEM, and NanoSIMS (fig. S1). The details for each analysis are as follows.

Samples

We used two polished Acfer 094 sections as samples. The areal sizes of the sections were ~6.6 mm^2 (Acfer 094 #1) and ~2.2 mm^2 (Acfer 094 #2) (fig. S2, A and C).

FE-SEM analysis

The two Acfer 094 polished sections were observed using an FE-SEM (equipped with a dual-beam FIB system, Thermo Fisher Scientific, Helios NanoLab G3, at Kyoto University) operated at 6 kV [process (1) in fig. S1]. The volume fractions of the major components (CAIs, chondrule, amoeboid olivine aggregate, and matrix) were calculated from whole-sample back-scattered electron (BSE) images. We colored each component in the BSE images and calculated a percentage of the colored area in the whole sample area using the Adobe Photoshop software package. This treatment was also applied to UPL (fig. S2, B and D). The size distribution of UPLs was obtained from the colored cross-sectional area (μm^2) of individual UPLs (fig. S3).

FIB microsampling

On the basis of the FE-SEM observations, specific portions were extracted from the polished sections for SR-XCT analyses using FIBs (Thermo Fisher Scientific, Helios NanoLab 3G CX and Quanta 200 3DS) at Kyoto University [process (2) in fig. S1]. Specific areas (~25 × 25 μm) were cut out to a depth of ~30 μm using a Ga^+ ion beam at 30 kV. Subsequently, the blocks were lifted from the polished sections and mounted on W-needles. The mounted samples were analyzed using SR-XCT [process (3) in fig. S1]. After the SR-XCT analyses, the samples were sliced into pieces for FE-TEM and NanoSIMS analyses using the FIBs [process (4) in fig. S1]. The sliced pieces were mounted on TEM grids and thinned to a thickness of 100 to 200 nm using a Ga^+ ion beam at 30 kV. The damaged layers that formed on the ultrathin sections were removed using a Ga^+ ion beam at 2 kV.

SR-XCT analysis

SR-XCT analyses were performed at BL 47XU of SPring-8, a synchrotron facility in Hyogo, Japan. SR-XCT permits the acquisition of a nondestructive 3D structure with high signal-to-noise ratios and high spatial resolution (~100 nm). We analyzed five samples by SR-XCT using two different methods, namely, DET and SIXM.

Dual-energy tomography

The DET is a method using x-ray absorption contrast for imaging (*10*), which provides a spatial distribution of x-ray LACs of materials as a digital image. The LAC values permit the identification of mineral

phases and their rough chemical compositions. The LAC value, μ, of a material is expressed as

$$\mu = \rho\Sigma\tau_i(E)w_i \quad (1)$$

where ρ is the density; $\tau_i(E)$ is the mass attenuation coefficient of element *i*, which is a function of the x-ray energy, *E*; and w_i is the weight fraction of element *i*. The relationship between LAC values and x-ray absorption is expressed as

$$I/I_0 = \exp(-\mu x) \quad (2)$$

where *I* and I_0 are the transmitted and incident x-ray beam intensities, respectively, and *x* is the sample size. As the LAC value obtained by reconstruction, μ_{CT}, is slightly smaller than the real value, μ, we provide the correction factor

$$\mu_{CT} = \gamma\mu \quad (3)$$

We corrected the LAC values using γ = 0.88, as obtained by calibration using standard materials.

In the DET, x-ray absorption images at two different x-ray energies were obtained. In this study, the two different x-ray energies were set to 7 and 8 keV, one above and one below the K-absorption edge energy of iron (7.11 keV). Using these two x-ray energies, the LAC values of most minerals in carbonaceous chondrites can be discriminated, whereas under a single energy, the LAC values of some pairs of minerals overlapped. The x-ray absorption contrasts at 7 keV corresponded closely to compositional (*Z*) contrasts, except for Fe, and those at 8 keV strongly depended on Fe content and were useful for checking the distribution of Fe-rich minerals (see Fig. 1, A and B).

An optical imaging system with a Fresnel zone plate (FZP) was used for resolving at a voxel size of 30 to 40 nm depending on the x-ray energy, which gives an effective resolution of ~100 nm. In the experiments, multiple projection images (1800 or 3600 projections) were taken by rotating the sample in small intervals through a total of 180° or 360° (0.1° per projection). 3D CT images were reconstructed from the projection images using a convolution back-projection algorithm.

Scanning imaging x-ray microtomography

SIXM is a hybrid tomography system consisting of a scanning x-ray microscope optical setup with a 1D focusing (line-focusing) device and an imaging x-ray microscope optical setup with a 1D objective (*11*). In our experiments, samples were illuminated with a line-focused beam, with the transmitted and deflected x-ray beams recorded in a 2D image detector. By rotating and scanning the samples with the line-focused beam, we simultaneously obtained both CT images of x-ray differential phase contrasts and x-ray absorption contrasts. The x-ray differential phase contrasts were derived from x-ray refraction in the samples and can be converted to the x-ray RID, δ, of an object, which is the difference between the x-ray refractive index, *n*, and unity

$$n = 1 - \delta \quad (4)$$

The RID value is expressed as

$$\delta = \rho\Sigma w_i\Delta_i(E) \quad (5)$$

where Δ_i is the mass RID of element *i*, which is a function of x-ray energy, *E*, and almost constant irrespective of the element species at constant *E* (Δ_i values for materials are available in the website http://henke.lbl.gov/optical_constants/). Therefore, the RID values were closely proportional to the density of the object, ρ. RID values are useful for discriminating air from those materials formed by light elements such as water and organics, which cannot be discriminated by LAC values alone in x-ray absorption images (see Fig. 1, D and E). In this study, the SIXM experiments were performed at 8 keV. Multiple projection images (750 projections) were taken by rotating the sample in small intervals through a total of 180° (0.24° per projection). Horizontal scan pitch was set to ~100 nm. Both phase and absorption CT images in 3D were reconstructed using a convolution back-projection algorithm. The voxel size of the CT images was ~100 nm, which gives an effective spatial resolution of several hundreds of nanometers. As an RID value obtained by the reconstruction, δ_{CT}, is slightly smaller than the real value, δ, we corrected the RID values using γ = 0.91 (considering γ in the same usage as in Eq. 3), which was obtained by calibration using standard materials.

Image processing and analysis

The voxel sizes of the DET images at 7 and 8 keV were slightly different from each other because we used an FZP. In SIXM, the voxel shape was not exactly a cube but strictly a quadrangular prism, and its edge sizes were different from the voxel size in DET. Therefore, we converted from the original CT images with the quadrangular prism voxel to those with cubic voxels using affine transformation. In addition, the rotation axis of each imaging experiment was not exactly the same, even if the same sample holder was used. Thus, image matching at common cubic voxel size and sample direction was required on different CT images of the same sample. For this image registration process, we used our original image processing method, where ~20 points per sample were selected as markers using the software package ImageJ, and well-matched CT image sets were produced by translation and rotation of 3D images based on the marker points. Using these CT image sets, we obtained both RID and LAC values for the same cubic voxel. This enabled us to identify the mineral phases in the CT samples and estimate their rough chemical compositions and densities (see Fig. 1, D and E).

FE-TEM/STEM-EDS observation and analysis

The ultrathin sections made from the XCT samples [process (4) in fig. S1] were analyzed using a field emission transmission electron microscope (JEOL, JEM 2100F, at Kyoto University) with an energy dispersive X-ray spectrometer (JEOL, JED-2300T) operated at 200 kV. TEM images were recorded using charge-coupled device (CCD) cameras (Gatan, Orius 200D and Orius 1000A) and analyzed using the software package Gatan Digital Micrograph. The porosity of UPLs (~40%) was estimated based on the TEM images (fig. S4). Crystal structural identification was based on SAED patterns. The SAED patterns were analyzed using the software package ReciPro (developed by Y. Seto). The 2D SAED patterns of amorphous silicates were converted to the 1D diffraction patterns using the software package IPA Analyzer (fig. S5) (*32*). In the conversion treatment, we removed the diffraction spots coming from the Fe—Ni sulfide inclusions. The 1D diffraction patterns were analyzed using the software package PDIndexer (*32*). We also acquired annular dark field STEM (ADF-STEM) images and x-ray elemental maps using the STEM-EDS system (Fig. 3, A to C, and fig. S6).

We performed quantitative chemical analyses using the STEM-EDS system. Elemental maps containing data of x-ray intensities in individual pixels were acquired by scanning a focused electron beam

with low beam current (1 to 2 pA) at a high speed (0.1 ms per point) to avoid the x-ray count decrement caused by electron beam irradiation damage. We confirmed that there was no obvious x-ray count decrement for each element in each map analysis. The x-ray intensities of all the major elements, including oxygen, were extracted from regions of interest in the maps and used for precise quantification. For the quantification, the ζ-factor method (*33*) was applied to the extracted x-ray intensity. Before quantification, the ζ factors of the instrument were characterized for all elements of interest using a thin-film sample of the National Institute of Standards and Technology SRM 2063a glass, according to protocols developed for the ζ-factor method (*33*). X-ray absorption correction was promoted significantly with this method because the ζ-factors were dependent only on the generated x-ray energy and accelerating voltage. A CCD camera (Gatan, Orius 200D) was used to hold the accurate electron beam current required for quantification. Error values were calculated according to procedures given by (*33*).

The estimation of the water content in the amorphous silicates was based on their chemical compositions obtained by the above method. The water content was calculated from the amount of oxygen excess based on the charge balance. In the calculation, we assumed the valence of iron to be $Fe^{3+}/\Sigma Fe = 0.66$ to 0.73 (*34*), and we assumed that sulfur and nickel were derived from Fe—Ni sulfide inclusions. We confirmed that anhydrous minerals (forsterite and enstatite) showed almost stoichiometric compositions without oxygen excess. The representative chemical compositions and estimated water contents of the amorphous silicates are shown in table S1.

NanoSIMS analysis

After the TEM analyses, one of the ultrathin sections was analyzed using NanoSIMS (Cameca, NanoSIMS 50L, at Kochi Institute for Core Sample Research) to obtain detailed isotopic characteristics. We also analyzed a relatively thick (~5 μm) sample extracted from a CT sample. A Cs^+ primary beam at 20 keV (~100 nm in diameter) was scanned over the sample areas of 12 × 12, 16 × 16, and 30 × 30 μm. The image resolution was set at 256 × 256 pixels for the 12 × 12– and 16 × 16–μm areas and at 512 × 512 pixels for the 30 × 30–μm area. The total exposure time was set to 0.05 to 0.1 s for each pixel for each analytical sequence. A normal incident electron flood gun was used to compensate for potential positive charging of the sputtered regions due to the primary beam. In each analytical sequence, we simultaneously obtained secondary ion images of $^{12}C^-$, $^{16}O^-$, $^{17}O^-$, $^{18}O^-$, $^{28}Si^-$, $^{32}S^-$, and $^{56}Fe^{16}O^-$. The oxygen isotopic compositions were calculated from the secondary ion counts extracted from the isotope images. The amorphous silicates and organics were selected from the isotope images based on the relative abundances of major elements. San Carlos olivine with known $^{18}O/^{16}O$ and $^{17}O/^{16}O$ ratios was used as the standard for the calculation. The oxygen isotopic compositions of the constituents of UPL and the matrix are summarized in table S3 and plotted in the oxygen three-isotope diagram (Fig. 3E).

SUPPLEMENTARY MATERIALS

Supplementary material for this article is available at http://advances.sciencemag.org/cgi/content/full/5/11/eaax5078/DC1

Fig. S1. Schematic illustration of the analytical protocol in this study.
Fig. S2. SEM images of the two Acfer 094 polished sections, #1 and #2.
Fig. S3. Histogram showing the size distribution of UPLs.
Fig. S4. BF-TEM image of a UPL.
Fig. S5. SAED patterns of amorphous silicates in UPLs and in the matrix.
Fig. S6. STEM-EDS maps of equilibrated aggregate–like objects in a UPL.
Fig. S7. BF-TEM image and SAED pattern of an enstatite whisker in the matrix.
Table S1. Compositions of GEMS-like materials in UPLs and in the matrix.
Table S2. Brief summary of textural and mineralogical characteristics of UPL, CP-IDP, and UPL-like lithology in the Paris meteorite.
Table S3. Oxygen isotopic compositions of UPL and matrix.

REFERENCES AND NOTES

1. J. P. Bradley, Analysis of chondritic interplanetary dust thin-sections. *Geochim. Cosmochim. Acta* **52**, 889–900 (1988).
2. L. P. Keller, S. Messenger, On the origins of GEMS grains. *Geochim. Cosmochim. Acta* **75**, 5336–5365 (2011).
3. J. P. Bradley, Chemically anomalous, preaccretionally irradiated grains in interplanetary dust from comets. *Science* **265**, 925–929 (1994).
4. J. P. Bradley, T. Ireland, The search for interstellar components in interplanetary dust particles. *Phys. Chem. Dyn. Interplanet. Dust* **104**, 275–282 (1996).
5. F. Kemper, W. J. Vriend, A. G. G. M. Tielens, The absence of crystalline silicates in the diffuse interstellar medium. *Astrophys. J.* **609**, 826–837 (2004).
6. R. van Boekel, M. Min, C. Leinert, L. B. F. M. Waters, A. Richichi, O. Chesneau, C. Dominik, W. Jaffe, A. Dutrey, U. Graser, T. Henning, J. de Jong, R. Köhler, A. de Koter, B. Lopez, F. Malbet, S. Morel, F. Paresce, G. Perrin, T. Preibisch, F. Przygodda, M. Schöller, M. Wittkowski, The building blocks of planets within the 'terrestrial' region of protoplanetary disks. *Nature* **432**, 479–482 (2004).
7. A. Greshake, The primitive matrix components of the unique carbonaceous chondrite Acfer 094: A TEM study. *Geochim. Cosmochim. Acta* **61**, 437–452 (1997).
8. H. Leroux, P. Cuviller, B. Zanda, R. H. Hewins, GEMS-like material in the matrix of the Paris meteorite and the early stages of alteration of CM chondrites. *Geochim. Cosmochim. Acta* **170**, 247–265 (2015).
9. J. N. Grossman, A. J. Brearley, The onset of metamorphism in ordinary and carbonaceous chondrites. *Meteorit. Planet. Sci.* **40**, 87–122 (2005).
10. A. Tsuchiyama, T. Nakano, K. Uesugi, M. Uesugi, A. Takeuchi, Y. Suzuki, R. Noguchi, T. Matsumoto, J. Matsuno, T. Nagano, Y. Imai, T. Nakamura, T. Ogami, T. Noguchi, M. Abe, T. Yada, A. Fujimura, Analytical dual-energy microtomography: A new method for obtaining three-dimensional mineral phase images and its application to Hayabusa samples. *Geochim. Cosmochim. Acta* **116**, 5–16 (2013).
11. A. Takeuchi, K. Uesugi, Y. Suzuki, Three-dimensional phase-contrast X-ray microtomography with scanning-imaging X-ray microscope optics. *J. Synchrotron Radiat.* **20**, 793–800 (2013).
12. C. Roosz, S. Grangeon, P. Blanc, V. Montouillout, B. Lothenbach, P. Henocq, E. Giffaut, P. Vieillard, S. Gaboreau, Crystal structure of magnesium silicate hydrates (M-S-H): The relation with 2:1 Mg-Si phyllosilicates. *Cem. Concr. Res.* **73**, 228–237 (2015).
13. J. P. Bradley, D. E. Brownlee, D. R. Veblen, Pyroxene whiskers and platelets in interplanetary dust: evidence of vapour phase growth. *Nature* **301**, 473–477 (1983).
14. G. Matrajt, S. Messenger, D. Brownlee, D. Joswiak, Diverse forms of primordial organic matter identified in interplanetary dust particles. *Meteorit. Planet. Sci.* **47**, 525–549 (2012).
15. R. N. Clayton, T. K. Mayeda, Oxygen isotope studies of carbonaceous chondrites. *Geochim. Cosmochim. Acta* **63**, 2089–2104 (1999).
16. N. Sakamoto, Y. Seto, S. Itoh, K. Kuramoto, K. Fujino, K. Nagashima, A. N. Krot, H. Yurimoto, Remnants of the early solar system water enriched in heavy-oxygen isotopes. *Science* **317**, 231–233 (2007).
17. L. R. Nittler, R. M. Stroud, J. M. Trigo-Rodríguez, B. T. De Gregorio, C. M. O' D. Alexander, J. Davidson, C. E. Moyano-Cambero, S. Tanbakouei, A cometary building block in a primitive asteroidal meteorite. *Nat. Astron.* **3**, 659–666 (2019).
18. A. Johansen, J. S. Oishi, M.-M. M. Low, H. Klahr, T. Henning, A. Youdin, Rapid planetesimal formation in turbulent circumstellar disks. *Nature* **448**, 1022–1025 (2007).
19. S. Okuzumi, H. Tanaka, H. Kobayashi, K. Wada, Rapid coagulation of porous dust aggregates outside the snow line: A pathway to successful icy planetesimal formation. *Astrophys. J.* **752**, 106 (2012).
20. A. Kataoka, H. Tanaka, S. Okuzumi, K. Wada, Fluffy dust forms icy planetesimals by static compression. *Astron. Astrophys.* **557**, 4 (2013).
21. J. M. Greenberg, Making a comet nucleus. *Astron. Astrophys.* **330**, 375–380 (1998).
22. K. Tsiganis, R. Gomes, A. Morbidelli, H. F. Levison, Origin of the orbital architecture of the giant planets of the solar system. *Nature* **435**, 459–461 (2005).
23. K. J. Walsh, A. Morbidelli, S. N. Raymond, D. P. Óbrien, A. M. Mandell, Populating the asteroid belt from two parent source regions due to the migration of giant planets—"The Grand Tack". *Meteorit. Planet. Sci.* **47**, 1941–1947 (2012).
24. S.-i. Sirono, Planetesimal formation induced by sintering. *Astrophys. J. Lett.* **733**, L41 (2011).

25. K. Ros, A. Johansen, Ice condensation as a planet formation mechanism. *Astron. Astrophys.* **552**, A137 (2013).
26. S. V. W. Beckwith, A. I. Sargent, Particle emissivity in circumstellar disks. *Astrophys. J.* **381**, 250–258 (1991).
27. A. Kataoka, T. Tsukagoshi, A. Pohl, T. Muto, H. Nagai, I. W. Stephens, K. Tomisaka, M. Momose, The evidence of radio polarization induced by the radiative grain alignment and self-scattering of dust grain in a protoplanetary disk. *Astrophys. J. Lett.* **844**, L5 (2017).
28. ALMA partnership, C. L. Brogan, L. M. Pérez, T. R. Hunter, W. R. F. Dent, A. S. Hales, R. E. Hills, S. Corder, E. B. Fomalont, C. Vlahakis, Y. Asaki, D. Barkats, A. Hirota, J. A. Hodge, C. M. V. Impellizzeri, R. Kneissl, E. Liuzzo, R. Lucas, N. Marcelino, S. Matsushita, K. Nakanishi, N. Phillips, A. M. S. Richards, I. Toledo, R. Aladro, D. Broguiere, J. R. Cortes, P. C. Cortes, D. Espada, F. Galarza, D. Garcia- Appadoo, L. Guzman- Ramirez, E. M. Humphreys, T. Jung, S. Kameno, R. A. Laing, S. Leon, G. Marconi, A. Mignano, B. Nikolic, L.-A. Nyman, M. Radiszcz, A. Remijan, J. A. Rodón, T. Sawada, S. Takahashi, R. P. J. Tilanus, B. Vila Vilaro, L. C. Watson, T. Wiklind, E. Akiyama, E. Chapillon, I. de Gregorio- Monsalvo, J. Di Francesco, F. Gueth, A. Kawamura, C.-F. Lee, Q. Nguyen Luong, J. Mangum, V. Pietu, P. Sanhueza, K. Saigo, S. Takakuwa, C. Ubach, T. van Kempen, A. Wootten, A. Castro- Carrizo, H. Francke, J. Gallardo, J. Garcia, S. Gonzalez, T. Hill, T. Kaminski, Y. Kurono, H.-Y. Liu, C. Lopez, F. Morales, K. Plarre, G. Schieven, L. Testi, L. Videla, E. Villard, P. Andreani, J. E. Hibbard, K. Tatematsu, The 2014 ALMA long baseline campaign: first results from high angular resolution observations toward the HL Tau region. *Astrophys. J. Lett.* **808**, L3 (2015).
29. S. Okuzumi, M. Momose, S.-i. Sirono, H. Kobayashi, H. Tanaka, Sintering-induced dust ring formation in protoplanetary disks: Application to the TL Tau disk. *Astrophys. J.* **821**, 82 (2016).
30. T. Zhang, X. Liang, C. Li, M. Lorin, Y. Li, L. J. Vandeperre, C. R. Cheeseman, Control of drying shrinkage in magnesium silicate hydrate (m-s-h) gel mortars. *Cem. Concr. Res.* **88**, 36–42 (2016).
31. J. D. Bass, Elasticity of Minerals, Glasses, and Melts, in *Mineral Physics & Crystallography: A Handbook of Physical Constants*, T. J. Ahrens, Ed. (American Geophysical Union, AGU Reference Shelf, 1995), vol. 2, pp. 45–63.
32. Y. Seto, D. Nishio-Hamane, T. Nagai, N. Sata, Development of a software suite on X-ray diffraction experiments. *Rev. High Pressure Sci. Technol.* **20**, 269–276 (2010).
33. M. Watanabe, D. B. Williams, The quantitative analysis of thin specimens: A review of progress from the Cliff-Lorimer to the new ζ-factor methods. *J. Microsc.* **221**, 89–109 (2006).
34. T. Hopp, C. Vollmer, Chemical compositions and iron oxidation state of amorphous silicates in the carbonaceous chondrite Acfer 094. *Meteorit. Planet. Sci.* **53**, 153–166 (2018).

Acknowledgments: We thank S. S. Russell and the Open University in Milton Keynes for providing the Acfer 094 samples, A. Hara for supporting the CT data processing, and A. Takigawa, T. Kim, and Y. Igami for the discussions. We also thank three anonymous reviewers for the helpful and constructive reviews. The SR-XCT experiments at SPring-8 in this study were conducted under the proposal nos. 2016A1245, 2016A1253, 2016B1350, 2016B1351, 2017A1442, 2017A1496, and 2017B1517. **Funding:** This study was supported by grant-in-aid no. 15H05695 for A.Ts., and nos. 18H04468 and 18K18795 for M.I. from the Japan Society for the Promotion of Science. **Author contributions:** All authors contributed equally to this work. M.M., A.N., A.M., and E.V. contributed to this paper mainly by SEM, TEM, and FIB works. A.Ts., J.M., K.U., A.Ta., and T.N. contributed to this paper by SR-XCT works. A.K. contributed to this work by discussions about theoretical planetesimal formation models. M.I., N.T., and Y.K. contributed to this work by NanoSIMS works. All the authors contributed to the discussions. **Competing interests:** The authors declare that they have no competing interests. **Data and materials availability:** All data needed to evaluate the conclusions in the paper are present in the paper and/or the Supplementary Materials. Additional data related to this paper may be requested from the authors. The software ReciPro, IPA Analyzer, and PDIndexer used for the TEM data analyses (developed by Y. Seto) are available in the website http://pmsl.planet.sci.kobe-u.ac.jp/~seto/.

Submitted 28 March 2019
Accepted 17 September 2019
Published 20 November 2019
10.1126/sciadv.aax5078

Citation: M. Matsumoto, A. Tsuchiyama, A. Nakato, J. Matsuno, A. Miyake, A. Kataoka, M. Ito, N. Tomioka, Y. Kodama, K. Uesugi, A. Takeuchi, T. Nakano, E. Vaccaro, Discovery of fossil asteroidal ice in primitive meteorite Acfer 094. *Sci. Adv.* **5**, eaax5078 (2019).

Science Advances

Discovery of fossil asteroidal ice in primitive meteorite Acfer 094

Megumi Matsumoto, Akira Tsuchiyama, Aiko Nakato, Junya Matsuno, Akira Miyake, Akimasa Kataoka, Motoo Ito, Naotaka Tomioka, Yu Kodama, Kentaro Uesugi, Akihisa Takeuchi, Tsukasa Nakano and Epifanio Vaccaro

Sci Adv **5** (11), eaax5078.
DOI: 10.1126/sciadv.aax5078